Research article

Novel starch-mediated synthesis of Au/ZnO nanocrystals and their photocatalytic properties

Boyan Peychev [a,b], Penka Vasileva [a,*]

[a] Faculty of Chemistry and Pharmacy, University of Sofia "St. Kliment Ohridski", 1 J. Bourchier, Sofia, 1164, Bulgaria
[b] School of Engineering and Materials Science, Queen Mary University of London, Mile End Road, London, E1 4NS, UK

ARTICLE INFO

ABSTRACT

A novel solution–solid synthesis method for preparation of ZnO and Au/ZnO composite nanocrystals using starch matrix has been developed and optimized. The process is characterized by simplicity, environmental compatibility and good performance. Nanocomposite samples with different gold content have been synthesized and studied with respect to their structure, size and shape of nanocrystals, thermal behavior, surface characteristics and optical properties, as well as their photocatalytic activity. We have found that modification of nanocrystalline ZnO with gold nanocrystals strongly influences the porosity of nanocomposites - less micro- and mesopores are formed, which results in a reduced specific surface area. The synthesized ZnO and Au/ZnO nanocrystals are active photocatalysts for the photocatalytic degradation of methylene blue (MB), as a model pollutant dye, in the UV region. There is a decrease in photocatalytic activity with an increase of the gold content in the nanocomposite photocatalyst. The degree of MB degradation obtained with a pure ZnO sample is comparable to that with the Au/ZnO photocatalyst with the lowest gold content 0.05 at. %. New and interesting result has been obtained relating to maximum specific (intrinsic) photocatalytic activity of 0.05 at. % Au/ZnO nanocrystals.

1. Introduction

Wastewater pollution is a big social and ecological problem stimulating worldwide research into pollution management and treatment [1, 2]. That is why remediation methods for dye pollution from the textile and paper industries are extensively researched. While many methods, like adsorption, reverse osmosis, chemical oxidation and others [3], could be used, with the development of nanomaterial sciences alternatives are sought after in the nanorealm [4].

One such alternative is photocatalytic degradation achieved through the use of nanostructured semiconductor particles, such as TiO$_2$, ZnO and so on [5, 6, 7, 8, 9, 10, 11, 12, 13, 14, 15]. Zinc oxide (ZnO) is perceived as a lower cost alternative photocatalyst to TiO$_2$ for the photodegradation of dyes and other organic compounds in aqueous solutions [16]. The fabrication of nanoorganized catalyst provides an effective way to overcome the relatively wide band gap as well as the high recombination rates of electron-hole pairs, photogenerated in ZnO [17, 18]. There are many different procedures used for synthesis of ultrafine oxide nanoparticles such as hydrothermal, sol-gel, solvothermal, emulsion precipitation, flame combustion, fungus mediated biosynthesis, etc [19, 20, 21, 22, 23, 24, 25, 26, 27]. A new, environmentally friendly and promising

approach in the metal oxide synthesis is the involvement of polysaccharides [28]. In wet and/or low-temperature synthesis methods, polysaccharides can play a multitude of roles (as complexing agent to avoid nanoparticles agglomeration, as assistant in heterogeneous nucleation to control the growth step or as surface capping agent), which has established them as attractive additives in material chemistry [29]. Among the polysaccharides, starch occupies a special position. It is unique with its abundance (the second biopolymer after cellulose), wide availability, low cost and functional flexibility.

Photocatalysts convert irradiational work into chemical work through their ability to interact in a specific way with light and matter. Having a free conduction band and small band gap, relative to isolators, semiconductors can generate excitons when illuminating with light from the ultraviolet-visible region of the spectrum [16, 30]. Photocatalytic degradation is a radical process which is initialized by the interaction between matter and the produced electron-hole pairs [31]. In aqueous solutions the catalyst generates hydroxyl and superoxide radicals which can react with the dye adsorbed on the catalyst surface, thus beginning the degradation process [32]. Figure 1 schematically illustrates the processes described.
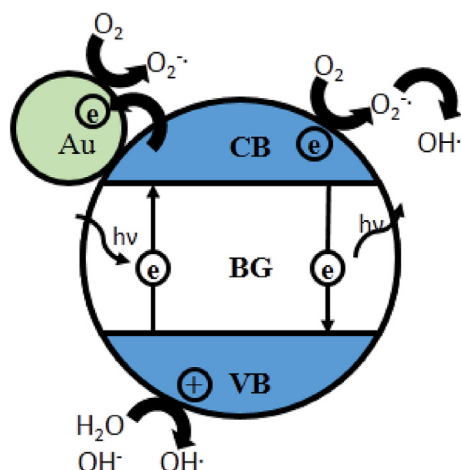
Figure 1. Schematic representation of the presumed photocatalytic process.

The addition of different noble metals to a photocatalyst has proven to be a possible way to increase the photocatalytic activity. The modifying metals facilitate charge transfer thus altering the catalysts electron spectra and overall properties [33]. In general by augmenting the catalyst in the described way the electron-hole pair recombinations are suppressed leading to a better photocatalytic performance [34]. Many efforts have been put into synthesizing semiconductor-noble metal nanocomposite materials in the recent years [35, 36, 37, 38, 39]. The advantages of Au over other noble metals has been reviewed and discussed [40] in terms of preparation methods, band offsets between ZnO and Au, photoluminescence properties, structural configurations of Au/ZnO, morphologically determined reactivity, dynamics of charge carriers, and photocatalytic reaction mechanisms associated with Au/ZnO.

In this article, we develop an innovative and effective solution–solid synthesis method for preparation of nanosized ZnO and Au/ZnO

photocatalysts in starch matrix. The study is directed towards: (i) Optimizing the starch-Zn source ratio for the preparation of nanosized ZnO photocatalyst; (ii) Producing Au-doped ZnO photoactive nanocomposite catalysts with different Au loading; (iii) Preforming an in-depth physicochemical characterization of the ZnO and Au/ZnO nanocomposite samples; (iv) Testing the UV photoassisted degradation of methylene blue (MB), as a model pollutant dye, using the obtained nanosized samples and commercial TiO_2 (Degussa P25) as photocatalysts.

2. Experimental

2.1. Materials

Zinc nitrate hexahydrate, $Zn(NO_3)_2.6H_2O$ (min. 99 %), tetrachloroauric(III) acid trihydrate, $HAuCl_4.3H_2O$ (min. 49 % Au), ethyl alcohol, C_2H_5OH (min. 99.7 %), soluble starch, $(C_6H_{10}O_5)_n$, and methylene blue (MB) were delivered bySigma-Aldrich. All reagents were used as supplied, without further purification. Bi-distilled water was used to prepare the solutions.

2.2. Preparation of pure ZnO and Au-doped ZnO nanocrystals

Pure ZnO and Au-doped ZnO nanocrystals were synthesized following a modified preparation procedure described in our previous study [41] and illustrated in Figure 2. Firstly, soluble starch (30 % w/V) was dissolved in warm distilled water (100 mL) under continuous stirring. Then, the desired amount of $Zn(NO_3)_2.6H_2O$ and $HAuCl_4.3H_2O$ (when applicable) was added in the above solution under vigorous stirring until complete dissolution. After heating at 90–100 °C with stirring at 1000 rpm for appropriate time period, the obtained clear and highly viscous solution was allowed to cool naturally to ambient temperature and subsequently incubated without any interruption at 4 °C for 40 h for complete gelation (*solution-phase stage*). The solvent was then replaced with ethanol and the solid formed was collected by microfiltration (MILIPORE, 0.2 μm), followed by successive washing with ethanol.
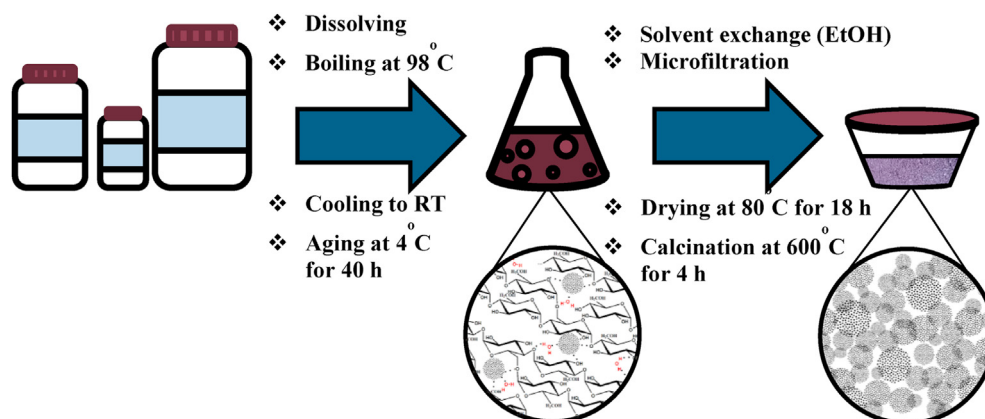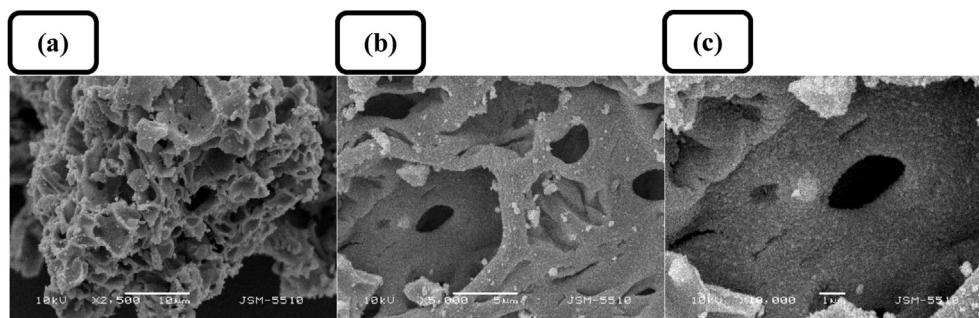

Figure 2. Typical solution-solid procedure utilized for preparation of nanosized ZnO and Au/ZnO.

Table 1. Symbols of the samples synthesized.

$c(Zn(II))$ in initial mixture, mol L^{-1}*	Au to Zn atomic ratio, at. % Au	Symbol of sample
0.5	-	Z1
0.1	-	Z2
1.5	-	Z3
0.5	0.05	A1Z1
0.5	0.10	A2Z1
0.5	0.50	A3Z1

* at constant amount of soluble starch - 30 % w/V.

Figure 3. Typical SEM images of ZnO sample Z1 at different magnifications and inset bars, respectively: (a) ×2500, 10 μm; (b) ×5000, 5 μm; (c) ×10000, 1 μm.

Finally, the solid was dried overnight in an oven at 80 °C, followed by calcination in an air atmosphere at 600 °C for 4 h (*solid-phase stage*). The resulting powders were stored in a desiccator at ambient temperature.

The Zn(II) concentration was varied to find the optimum starch to Zn(II) source mass ratio for the synthesis of nanosized catalyst with high photocatalytic activity and maximum yield. Three different Zn(II) concentrations were studied: 0.5 mol L^{-1} – the sample was denoted as Z1; 1.0 mol L^{-1} – sample Z2; 1.5 mol L^{-1} – sample Z3 (see Table 1). Using the Z1 sample configuration, 30 % w/V starch and 0.5 mol L^{-1} Zn(II), Au enhanced photocatalysts were prepared by adding various proportion of $HAuCl_4.3H_2O$ to the definite amount of Zn(II). Three different Au to Zn atomic ratios were studied: 0.05 at. % – sample A1Z1; 0.1 at. % – sample A2Z1; 0.5 at. % – sample A3Z1 (see Table 1).

2.3. Physicochemical characterization of the photocatalysts

The thermal behavior of dry solid precursors was analyzed using thermogravimetric measurements (TG/DTA) (STA Stanton Redcroft 1500) in the range of 20–750 °C with a heating rate of $10°$ min^{-1}.

The structural properties and morphology of ZnO and Au/ZnO synthesized samples were analyzed using X-ray diffraction analysis (XRD), scanning-electron microscopy (SEM, JEOL JSM-5510), and high-resolution (HR) transmission-electron microscopy (TEM) with selected area electron diffraction (SAED). X-ray diffractograms of the samples were recorded with a Siemens D500 diffractometer. The diffractograms are in the 2θ angle range from $20°$ to $90°$. The wavelength λ of the incident radiation is 0.15418 nm (Cu Kα line). The average size of crystallites was calculated using Scherrer's equation (Eq. 1) from the broadening of (101) peak (2θ = 36.4°) in the sample diffractograms. SEM micrographs of the samples, from which the surface morphology were observed, were captured by a JEOL JSM-55 scanning electron microscope. The samples were prepared by dispersing in water under sonication, and depositing on a glass slide. Furthermore, the sample slides were air dried at ambient temperature for 24 h and consecutively gold coated under vacuum. The average size and shape of the particles in the samples were obtained from (HR)TEM micrographs captured by a JEOL 2100 high-resolution transmission electron microscope operating at an accelerating voltage of 200 kV. The samples for TEM microscopic analysis were dispersed in water by sonication and dropped on a carbon-coated copper grid, then air-dried at ambient temperature for 24 h.

Nitrogen adsorption–desorption isotherms were recorded in a Quantachrome Instruments NOVA 1200e (USA) apparatus at low-temperature (77.4 K). Prior to measurement, all samples were out-gassed in deep vacuum and high temperature (50 °C) for 16 h. From the physisorption isotherms, the specific surface areas (S_{BET}) and total pore volume (V_t) were calculated using the BET equation and the Gurvich rule, respectively (at high relative pressure). The pore size distributions were evaluated from the desorption branches of isotherms using the BJH method.

The optical and photochemical properties were analyzed through UV-Vis absorption spectroscopy and photoluminescence (PL) spectroscopy.

UV-Vis absorption spectra were recorded in aqueous dispersions using a Thermo Scientific Evolution 300 UV–Vis spectrophotometer with 1 cm optical path cell. The electronic bands structures of the samples were discerned from the photoluminescence spectra, recorded in dichloromethane dispersion using a Perkin Elmer LS45 fluorescence spectrometer with a pulsed xenon light source and excitation wavelength of 325 nm.

2.4. Photocatalytic activity test

Methylene blue dye, representative of the most important pollutants in the textile industry wastewater, was used as a model system. The photocatalytic activity of the studied samples was evaluated through the degradation of MB dissolved in water with definite content (10 ppm) under UV irradiation. The light source was a UV lamp (Sylvania 18 W BLB T8), emitting in the range 315–400 nm. The lamp was located at 10 cm above the treated solution and the temperature was kept at room levels. The reactor set up was covered with black color plastic hood to prevent photopollution into the system. The volume of dye solution was 100 mL into which 100 mg of photocatalyst were added under continuous magnetic stirring to achieve a homogeneous distribution of the photocatalyst in the suspension. The suspension was magnetically stirred in dark conditions for 30 min to achieve adsorption–desorption equilibrium between catalysts and MB molecules. Afterwards, the dispersion was putted under the UV light. Sampling was performed at regular intervals (every 10 min) with a syringe in order to monitor the dye degradation process. Aliquots of 1 mL suspension were withdrawn and centrifuged for 10 min. The residual concentration of MB was determined by measuring the absorption spectra of supernatants using an UV-Vis spectrophotometer. The maximum absorption intensity of the band at 664 nm corresponds to the amount of MB present and thus, determines the photoactivity of the catalysts. No change in dye concentration was recorded (within the error limit of measurement) at the same conditions, but without photocatalyst. For comparison, the commercial product TiO_2 Degussa P25 was also tested as a photocatalyst in this study at the described conditions.

3. Results and discussion

3.1. Physicochemical characteristics of pure ZnO samples

SEM was applied to study the surface morphology of the pure ZnO samples. Changing the Zn(II) concentration at constant amount of starch produces a negligible effect on the surface morphology. Typical SEM micrographs of Z1 sample (top views), obtained at different magnifications and presented in Figure 3, show that the powder sample exhibits a highly porous surface structure determined by the removal of starch template in the calcination step. The N_2 adsorption–desorption isotherms of pure ZnO samples are Type V with characteristic hysteresis loops of a blended type between type H1 and H2, which signify the presence of a micro-meso porous structure (Figure 4a). The BET analysis revealed that, regardless of the different values of starch – Zn(II) source mass ratio, the
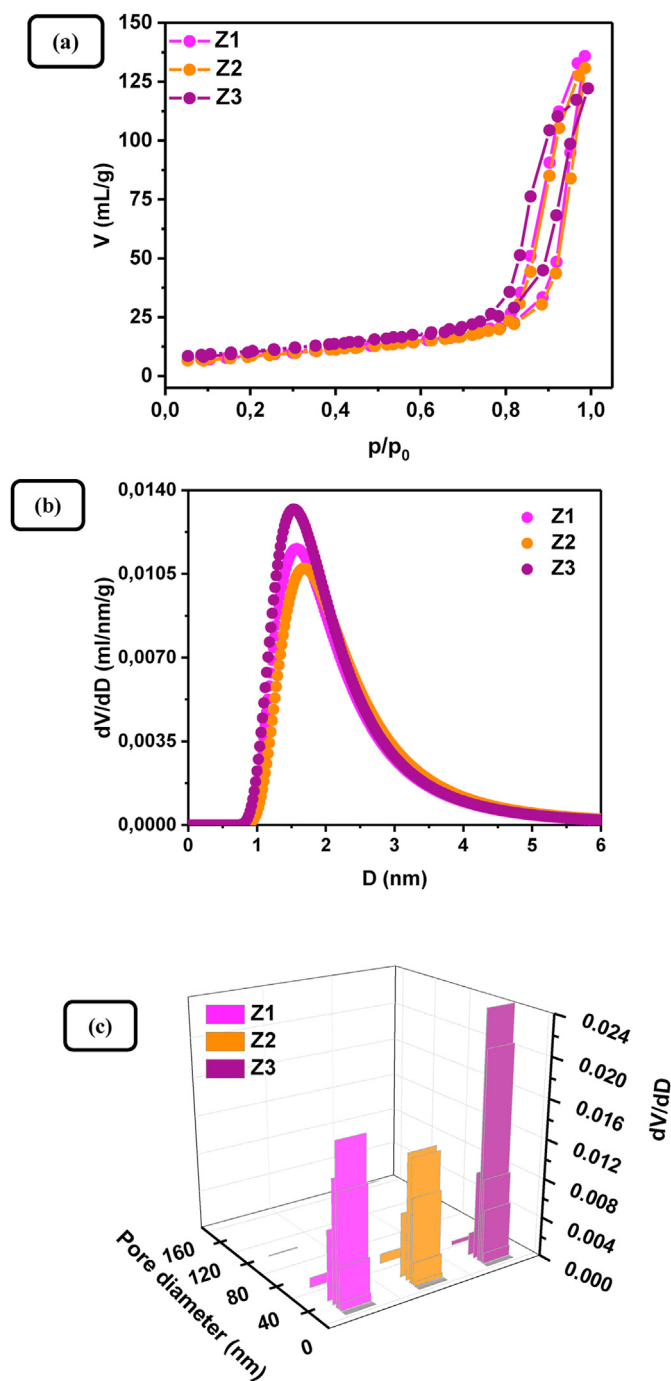
Figure 4. (a) N$_2$-adsorption-desorption isotherms of ZnO samples Z1, Z2, and Z3, (b) and (c) Desorption dV/dD distributions vs pore diameter for micropores and mesopores, respectively.

values of specific surface area of the synthesized samples do not show an orientated deviation from an average, at least for the studied Zn(II) concentration range; the specific surface area values are 33 m^2 g^{-1}, 31 m^2 g^{-1}, and 37 m^2 g^{-1} for the samples Z1, Z2, and Z3, respectively. Compared to the specific surface area of commercial ZnO powders (ca. 4–5 m^2 g^{-1}), these values are relatively higher, but they are comparable to the values obtained for multilayered ZnO nanosheets with hierarchically porous structures [42] and hierarchically assembled ZnO nanoflakes [43]. The BJH pore size distribution curves and diagrams (Figure 4b and c) reveal that the pure ZnO samples synthesized with different Zn(II) to starch mass ratios possess average pore sizes in the

range of 20–26 nm and total pore volumes – in the range of 0.19–0.21 cm^3 g^{-1}.

The microstructure of the prepared pure ZnO samples was further studied by TEM and HRTEM. From typical TEM and HRTEM micrographs of Z1 samples depicted in Figure 5, it can be concluded that the pure ZnO consist of mostly spherical nanoparticles with an average particle size of 15.4 $\pm$ 2.8 nm (also proved by XRD) and a relatively narrow size distribution. The SAED pattern, presented in Figure 5a (inset), confirms the polycrystalline nature of the nanosized ZnO product. HRTEM observation shows a high crystallinity of the nanostructured ZnO product (Figure 5b). The lattice spacing of 0.247 nm is indexed to the (101) planes of hexagonal crystalline ZnO, wurtzite structure (JCPDS 36–1451). It is obvious that the starch matrix plays a key role in the product formation. The large number of coordinating functional groups in the starch structure determines the formation of starch-Zn(II) complexes that are surface-active sites of nucleation and initial crystal growth of ZnO [44], and probably influences the size and aggregation state during the particle growth process [45, 46].

The crystal structure of the pure ZnO samples was studied by XRD. The XRD patterns of the samples exhibit seven peaks as shown in Figure 6. These diffraction peaks at 2θ of 31.8°, 34.5°, 36.4°, 47.6°, 56.7°, 62.9° and 68.1° correspond to the (100), (002), (101), (102), (110), (103) and (112) crystal planes, respectively, of hexagonal wurtzite crystals ZnO (JCPDS 36–1451). The size of the crystallites (D_{XRD}) presented on Table 1 was determined by Scherrer's formula (Eq. 1):

$$D_{XRD} = (k \times \lambda)/(\beta \times \cos\theta) \tag{1}$$

where k is a constant assumed equal to 0.94, λ is the wavelength of the Cu Kα radiation, β is the full width at half-maximum (FWHM) intensity of the peak, and θ is the Bragg angle of the peak. The average crystallite size of 14.3 nm, 15.4 nm, and 14.3 nm was calculated for sample Z1, Z2, and Z3, respectively, which is in a good agreement with the average particle diameter obtained by TEM analysis (15.4 $\pm$ 2.8 nm for pure ZnO sample Z1).

In order to further characterize the pure ZnO nanocrystals, room-temperature photoluminescence (PL) spectra and UV–Vis absorption spectra of the nanosized samples were recorded and depicted in Figures 7a and 7b, respectively. The near-band-edge-emission at 385 nm is clearly present and can be attributed to the exciton transition. Its superior intensity indicates high purity and crystallinity of nanocrystalline ZnO products. The other bands observed in PL spectra at 425 nm (blue emission), 485 nm (blue–green emission), and 530 nm (green emission) are usually associated with surface defects and oxygen vacancies [47, 48, 49]. The nanosized ZnO samples prepared in starch template at different Zn(II) concentrations exhibit a sharp absorption band at around 374 nm and a relatively steep slope of the absorption curve confirming an appreciable crystalline quality [50], which agrees well with the XRD data, PL-measurements, and HRTEM observations. The pure ZnO samples also show light absorption in the visible region from 420 to 600 nm, probably caused by defects as reported by Cheng et al. [51].

3.2. Physicochemical characteristics of Au-doped ZnO samples

All Au-doped ZnO samples were synthesized using Zn(II) concentration corresponding to pure ZnO sample marked as Z1, because of the fact that among all pure ZnO samples, the sample Z1 is the most active photocatalyst in the studied reaction.

The formation of gold nanoparticles during the heating process of reaction mixture was monitored using UV-Vis absorption spectroscopy. Appearance of Au NP surface plasmon resonance (SPR) band and evolution of the absorption intensity at λ$_{max}$ was detected in the UV-Vis absorption spectrum (Figure 8). In the wavelength range of 350–800 nm, the SPR band of gold nanoparticles at ~540 nm is directly observable and corresponds to the change of mixture color in the heating process. After 90 min heating time, the SPR band widens, towards lower
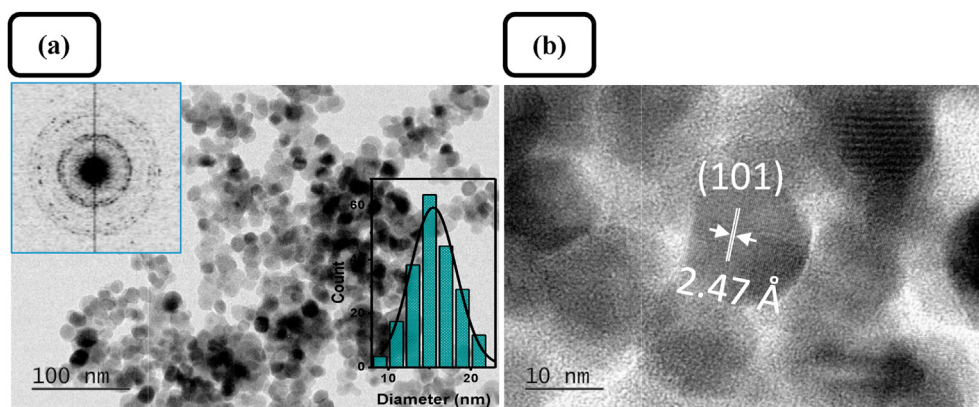
Figure 5. (a) Typical TEM and (b) HRTEM images of ZnO sample Z1; insets in (a): SAED pattern and size distribution histogram.
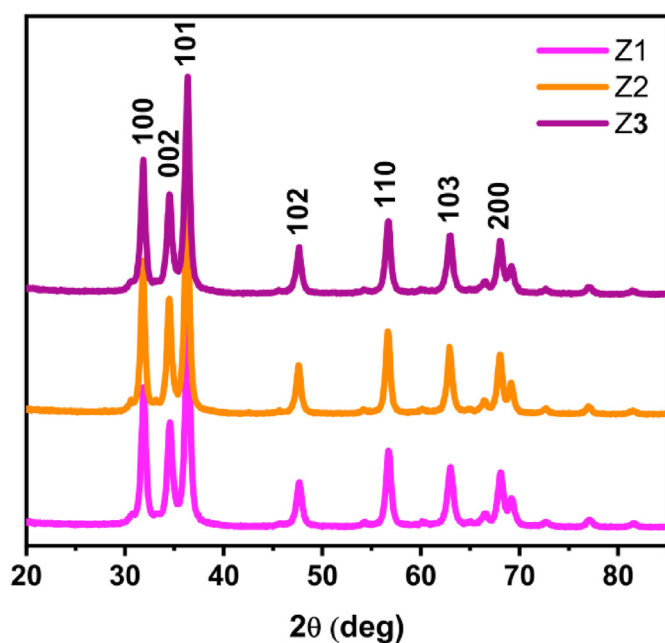

Figure 6. XRD patterns of ZnO samples Z1, Z2, and Z3; the indices above the peaks show the corresponding diffracting planes of ZnO (JCPD 36–1451).

Figure 10. The highly porous structure characteristic of the non-modified samples is observable in the Au-loaded ZnO samples as well. Nitrogen adsorption–desorption isotherms were determined in order to evaluate the specific surface area and pore size distribution of Au-loaded ZnO samples compared to those of pure ZnO sample Z1 (Figure 11). Similar to the samples of pure ZnO, the Au/ZnO samples exhibited type V isotherms of types H1 and H2 hysteresis loops (Figure 11a). A monotonic decrease
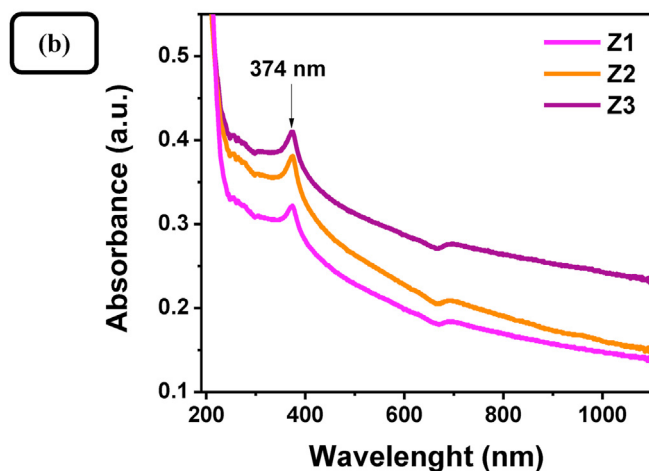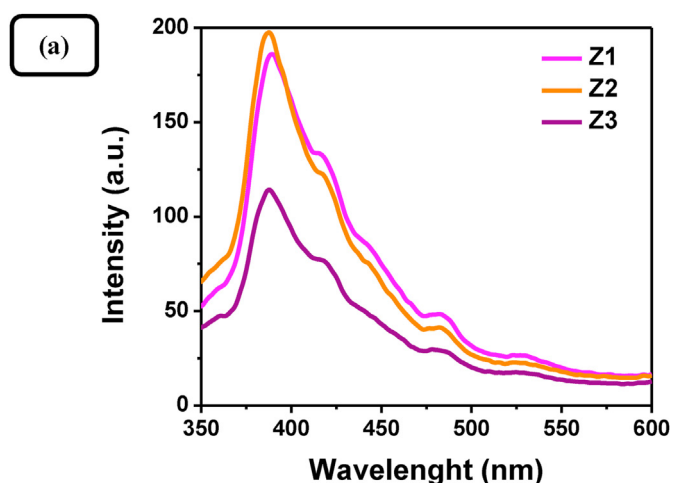

Figure 7. (a) Room temperature photoluminescence spectra and (b) UV–Visible absorption spectra of ZnO samples Z1, Z2, and Z3 dispersed in dichloromethane and water, respectively.

frequencies, indicating particle agglomeration. Therefore, the optimal heating time in the solution stage of the developed procedure for preparation of hybrid Au-doped ZnO nanocrystals is 90 min.

Thermogravimetric and differential thermal analysis (TG/DTA) of the gel solids, isolated by microfiltration and dried at 80 °C, were used to further characterize the thermal behavior of ZnO–starch and Au/ZnO–starch composites (uncalcinated samples). As can be seen from Figure 9a, three stages of weight loss are observed, corresponding to dehydration and two-step starch degradation. No weight loss between 500 and 800 °C was detected on the TG curve of samples studied, which suggests the formation of nanocrystalline ZnO as the decomposition product [52]. The two starch degradation bands, observable in the thermogram of pure starch (Figure 9b), merge into one with the addition of Zn(II) into the system due to its catalytic effect on starch decomposition [53] and the phase formation between 300 and 480 °C assigned to ZnO crystallization and crystal growth. The band corresponding to gold phase transformation (300–500 °C) is not observed, because of its relatively small intensity compared with the starch degradation and ZnO formation bands in the same temperature interval.

The addition of gold does not have a noticeable effect on the surface morphology of the samples as can be seen from the SEM images shown in

Figure 8. UV-Visible absorption spectra of diluted reaction mixture starch-Zn(II)–Au(III) at different lengths of heated mixing.

in the specific surface area is observed for the Au-loaded samples corresponding to the increase of the gold concentration. The effect can be related to both acid hydrolysis of the polysaccharide matrix in the synthetic process leading to a lesser degree of polymerization and electrostatic screening from the tree-valent ions resulting in a contraction of the polymeric backbone. The specific surface areas are found to be 26 m^2 g^{-1}, 23 m^2 g^{-1}, and 12 m^2 g^{-1} for the samples A1Z1, A2Z1, and A3Z1, respectively (Figure 11a). As can be seen on Figure 11b and c, the samples are micro-meso porous (average pore sizes in the range of 21–27 nm) and the pore distribution type is not affected by the modification of ZnO with gold nanocrystals. Nevertheless, the total pore volume diminishes with the addition of gold (from 0.14 cm^3 g^{-1} for A1Z1 sample to 0.08 cm^3 g^{-1} for A3Z1 sample).

The TEM and HRTEM images (Figure 12) of Au-doped ZnO samples show an identical nanoorganized structure as in the pristine ZnO sample Z1. Uniform spherical nanoparticles can be observed with slightly larger, compared to the pristine one, average particle size of 18.9 ± 3.5 nm. The product has a polycrystalline structure as proved from the SAED pattern (Figure 12a, inset). On the HRTEM image an Au and ZnO nanosized crystals of relatively similar size can be seen side by side. The lattice spacings of 0.274 nm and 0.235 nm are indexed to the (100) planes of hexagonal wurtzite crystalline ZnO (JCPDS 36–1451) and (111) planes of face-centered cubic Au (JCPDS 04–0784), respectively. These results showed that shape, size and organization of ZnO nanoparticles in Au-doped ZnO samples are not affected by the gold loading.

The crystal phases of the Au-doped ZnO samples are characterized by XRD. As shown in Figure 13, the XRD patterns show diffraction peaks of both hexagonal wurtzite ZnO and face-centered cubic Au. The peaks are relatively wide and short, typical for a nanosized system. The peaks at 31.8°, 34.5°, 36.4°, 47.6°, 56.7°, 62.9° and 68.1° corresponding to (100), (002), (101), (102), (110), (103), and (112) crystal planes, respectively, of the wurtzite ZnO phase (JCPDS 36–1451), experience no change in their position with the addition of gold, with respect to the Z1 sample, suggesting that solid solutions are not formed and the gold does not integrate into the wurtzite structure. Furthermore, the calculated lattice parameters (Table 2) for the zinc oxide structure are in agreement with that conclusion, showing no significant difference for the synthesized samples. The crystallite sizes were calculated for the metal oxide phase to be 18.5 nm, 18.8 nm and 19.2 nm for the samples A1Z1, A2Z1, and A3Z1, respectively. The intensity of peak at 38.1°, 42.2° and 64.4°,

corresponding to (111), (200) и (220) crystal planes, respectively, of Au nanophase (JCPDS 04–0784), increases with the increase of the gold content in Au-doped ZnO samples. No characteristic peaks for impurities were observed, which proved the high purity of the final products.

Photoluminescence spectra of Au-doped ZnO samples depicted in Figure 14 are qualitatively the same as those of the unmodified ones (Figure 7a). The bands at 385 nm, 425 nm, 485 nm and 530 nm are again observed and indicate high purity and crystallinity of the products. A suppression of the photoluminescence is present for the Au-doped samples in respect to the corresponding pristine ZnO sample Z1, which is most likely due to the stabilization of the electron-hole pairs in the presence of gold, with the exception of sample A3Z1. The different behavior of the sample with highest gold concentration, can be justified with the ability of the metal particles to act as recombination centers, determined by the higher probability of hole transfer to a negatively charged metal nanoparticle [54].

3.3. Photocatalytic properties

In order to evaluate the photoactivity of nanosized ZnO and Au/ZnO photocatalysts prepared, the photocatalytic degradation of MB was studied in a semi-batch type reactor. The appropriate amount of catalyst was dispersed into 100 mL MB solution with dye concentration of 10 ppm
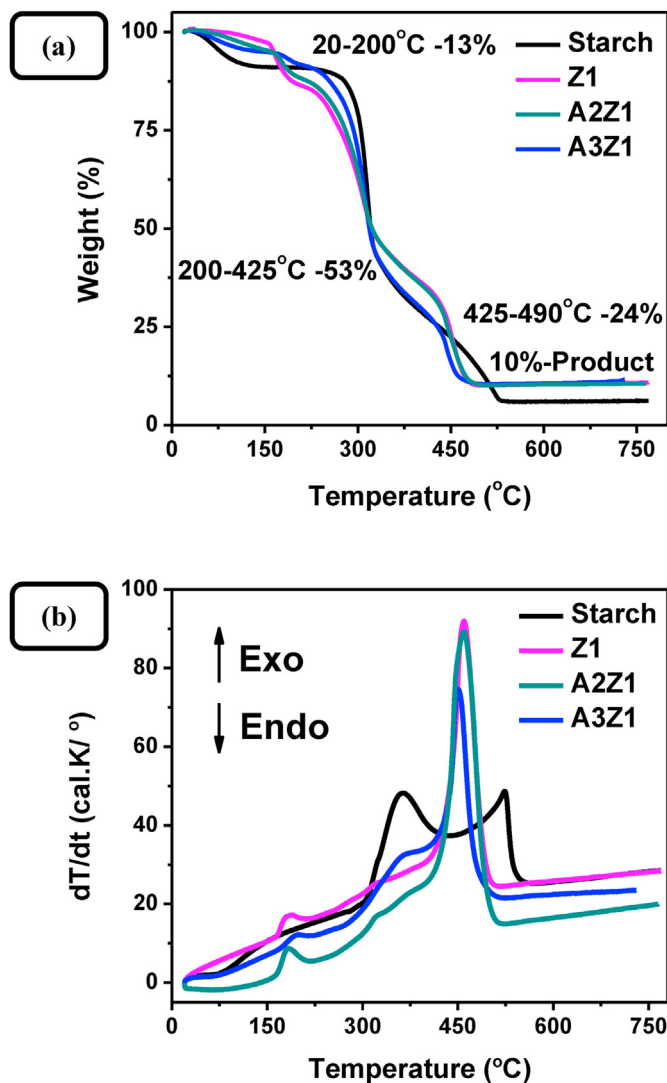
Figure 9. Thermogravimetric and differential thermal analysis of starch and dry precursor gels for samples Z1, A2Z1, and A3Z1.
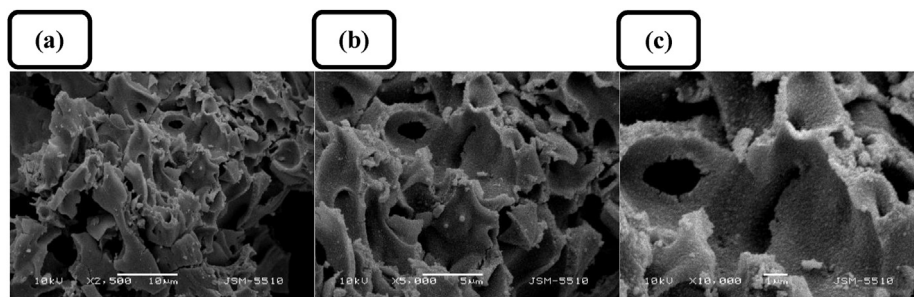
Figure 10. SEM images of sample A2Z1 at different magnifications and inset bars, respectively: (a) ×2500, 10 μm; (b) ×5000, 5 μm; (c) ×10000, 1 μm.

and placed in an open photocatalytic reactor with free access to atmospheric oxygen. The suspension is kept in dark condition for 30 min designated as *dark period*. Then the lamp is turned on and samples are taken for UV-Vis analysis at intervals of 10 min. In this highly diluted system, the ratio of absorption intensity of MB A_t at irradiation time t to the value A_0 measured at $t = 0$ should be equal to the concentration ratio c_t/c_0 of MB. Furthermore, at low dye concentration and large stoichiometric excess of dissolved oxygen, a pseudo-first-order reaction kinetics (Eqs. (2) and (3)) with respect to MB is to be expected [54, 55, 56]. The kinetic equation for the reaction can be written as:

$$dc_t/dt = -k_{app}c_t \qquad (2)$$

$$\ln c_t/c_0 = \ln A_t/A_0 = -k_{app}\,t \qquad (3)$$

where c_t is the concentration of MB at irradiation time t, k_{app} is the apparent pseudo-first-rate kinetic constant.

As can be seen from Figures 15a and 16a, during the dark period there is an initial drop of intensity corresponding to adsorption of the dye followed by a slow rise due to desorption. From previous studies it was determined that 30 min is adequate time to reach equilibrium conditions. While the kinetics of sorption is on the same timescale as the photodegradation, the amount of adsorbed dye is quite low. Thus, the adsorption plays a negligible role in the total concentration drop observed upon irradiation for 90 min. Similar data on negligible adsorption of dye molecules on the catalyst surface have been already reported in the literature [57, 58].

The plot $\ln A_t/A_0$ versus irradiation time t (Figures 15b and 16b) is linear, revealing that the photocatalytic degradation reaction follows pseudo-first-order reaction kinetics (Eq. 3) with respect to MB, as is commonly found in the literature. The kinetics results testify that the photocatalytic activity of nanosized ZnO samples Z1, Z2, Z3 increases with increasing starch – Zn(II) source mass ratio. Moreover, the photoactivity of all nanosized ZnO photocatalysts synthesized by the here presented method is greater than that of commercial TiO$_2$ photocatalyst (Degussa P25). The apparent reaction rate constants were evaluated from the slope of $\ln A_t/A_0$ versus t plots. Values of the apparent pseudo-first-rate kinetic constants (k_{app}) and squares of linear correlation coefficients (R^2) are reported in Table 3. Obviously, the value of apparent rate constant decreases from 0.03823 to 0.02554 min^{-1} as the Zn(II) concentration increases from 0.5 to 1.5 mol L^{-1}. The intrinsic activity (Table 3), defined as the apparent rate constant divided by the BET specific surface area of the respective photocatalyst, shows a monotonic decrease with the increase of starch – Zn(II) source mass ratio as well.

As seen from Figures 16a and 16b the photocatalytic activity of the gold-doped ZnO nanocrystals decreases with the increase of Au concentration, directly correlating to the specific surface area values. Similar results have been already published in the literature [18]. Obviously the less developed surface area of photocatalysts, offering less active sites for the photocatalytic process, plays a limiting role on the increase of catalytic activity through the developed method. On the other hand, the intrinsic activity (Table 3) shows an irregular change
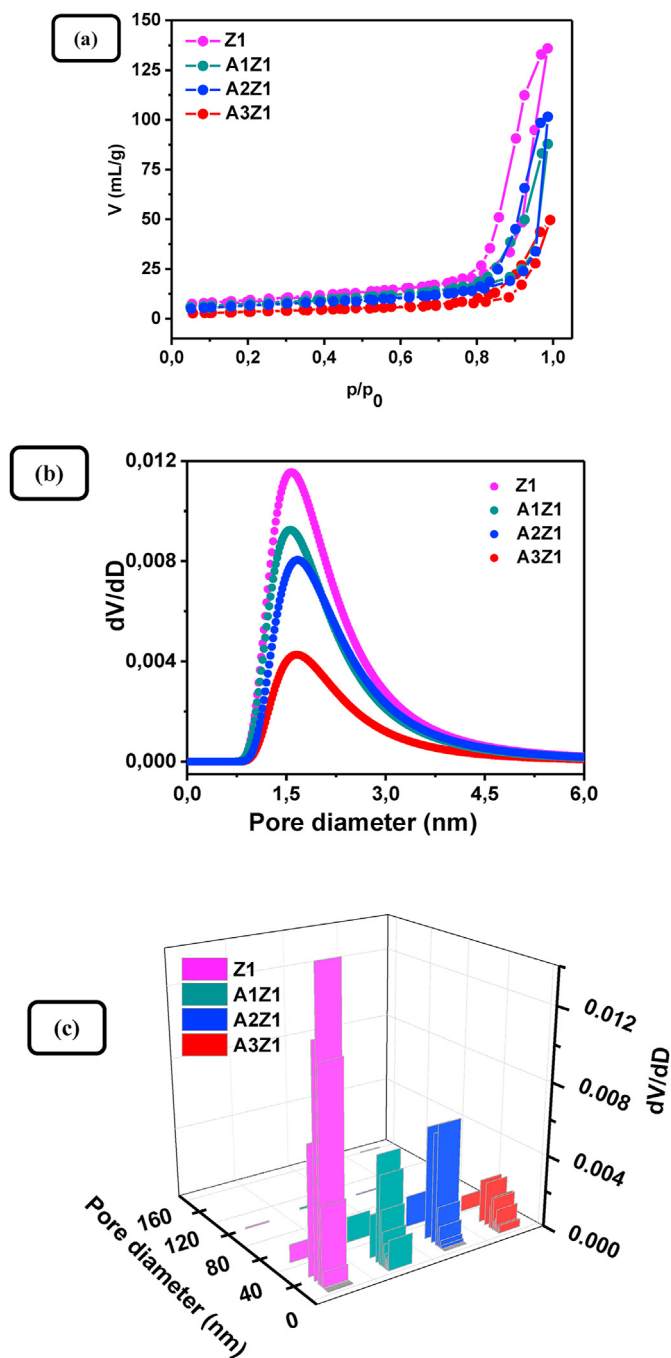
Figure 11. (a) N$_2$-adsorption-desorption isotherms of Z1 sample and A1Z1, A2Z1, A3Z1 samples, (b) and (c) Desorption dV/dD distributions vs pore diameter for micropores and mesopores, respectively.
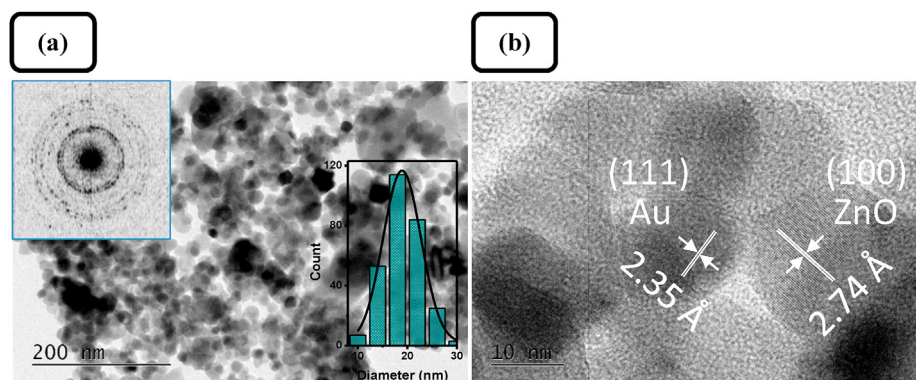
Figure 12. (a) TEM and (b) HRTEM images of sample A2Z1; insets in (a): SAED pattern and size distribution histogram.
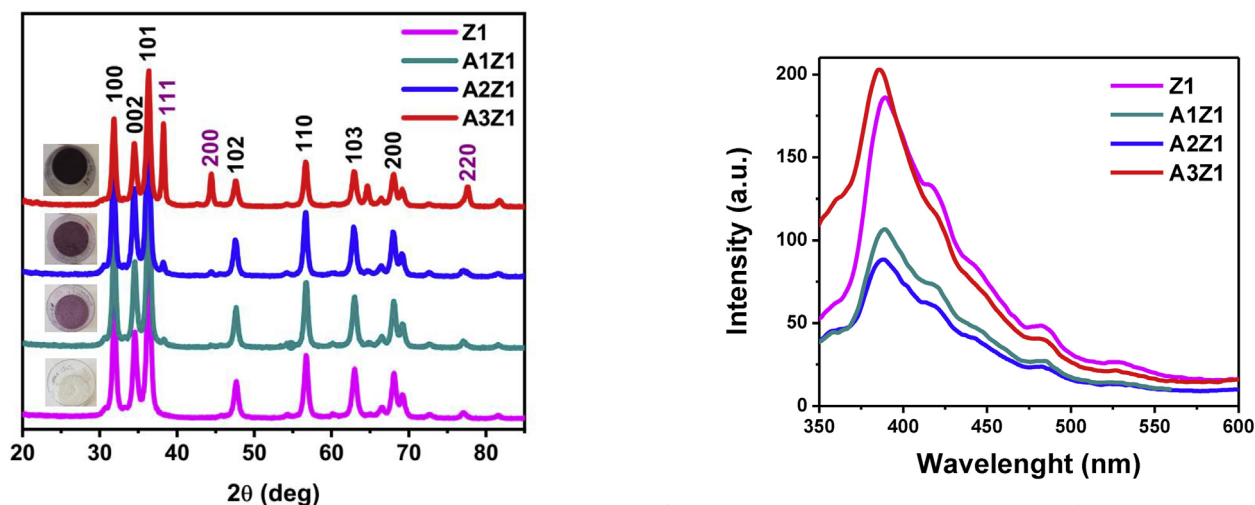

Figure 13. XRD patterns with digital photos of samples Z1, A1Z1, A2Z1, and A3Z1; the indices above the peaks show the corresponding diffracting planes of ZnO (in black color, JCPD 36–1451) and Au (in magenta color, JCPD 80-0075).

Figure 14. Room temperature PL spectra of samples Z1 and A1Z1, A2Z1, A3Z1 dispersed in dichloromethane.

Table 2. Average crystallite size calculated by Scherer's formula and lattice parameters of the crystal structure of ZnO.

Sample	Crystallite size		Cell parameters	
	D_{XRD}, nm	SD, nm	a, Å	c, Å
Ref. 36-1451	-		3.2509	5.2071
Z1	14.3	0.1	3.2409	5.1924
Z2	15.4	0.2	3.2483	5.2025
Z3	14.3	0.2	3.2464	5.1985
A1Z1	18.5	0.1	3.2440	5.1958
A2Z1	18.8	0.1	3.2515	5.2082
A3Z1	19.2	0.1	3.2476	5.2025

with the gold content, being higher for two of the synthesized samples. While many factors play a role on catalytic activity the higher values of the intrinsic activity, corresponding to samples A1Z1 and A3Z1, suggest a synergism between the ZnO and Au nanophases. The difference in the photocatalytic activity of pure ZnO and Au-doped nanocrystals synthesized can also be partially attributed to different type and quantity of pores present in the sample. The observed hysteresis in the adsorption-desorption isotherms forms mainly as a result of a nucleation delay of the capillary condensation and "pore blocking" where larger pore "bodies" empty through smaller pore "necks". Thus the

relatively wider loops of samples Z3 and A2Z1, with respect to the other synthesized samples, suggest an increased amount of "ink-bottle" pores, which could explain the deviation of the A2Z1 sample from the trend. Because the narrow "mouths" of the "ink-bottle" pores play a limiting role on the sorption processes, the overall kinetics of the photocatalytic reaction is thereby slowed down.

Furthermore, Figure 17 presents the typical variation of absorption spectrum of MB solution during the photooxidative process catalyzed by the synthesized nanosized ZnO samples. The intensity of bands at 664, 246 and 292 nm, which are present originally on the MB spectrum,
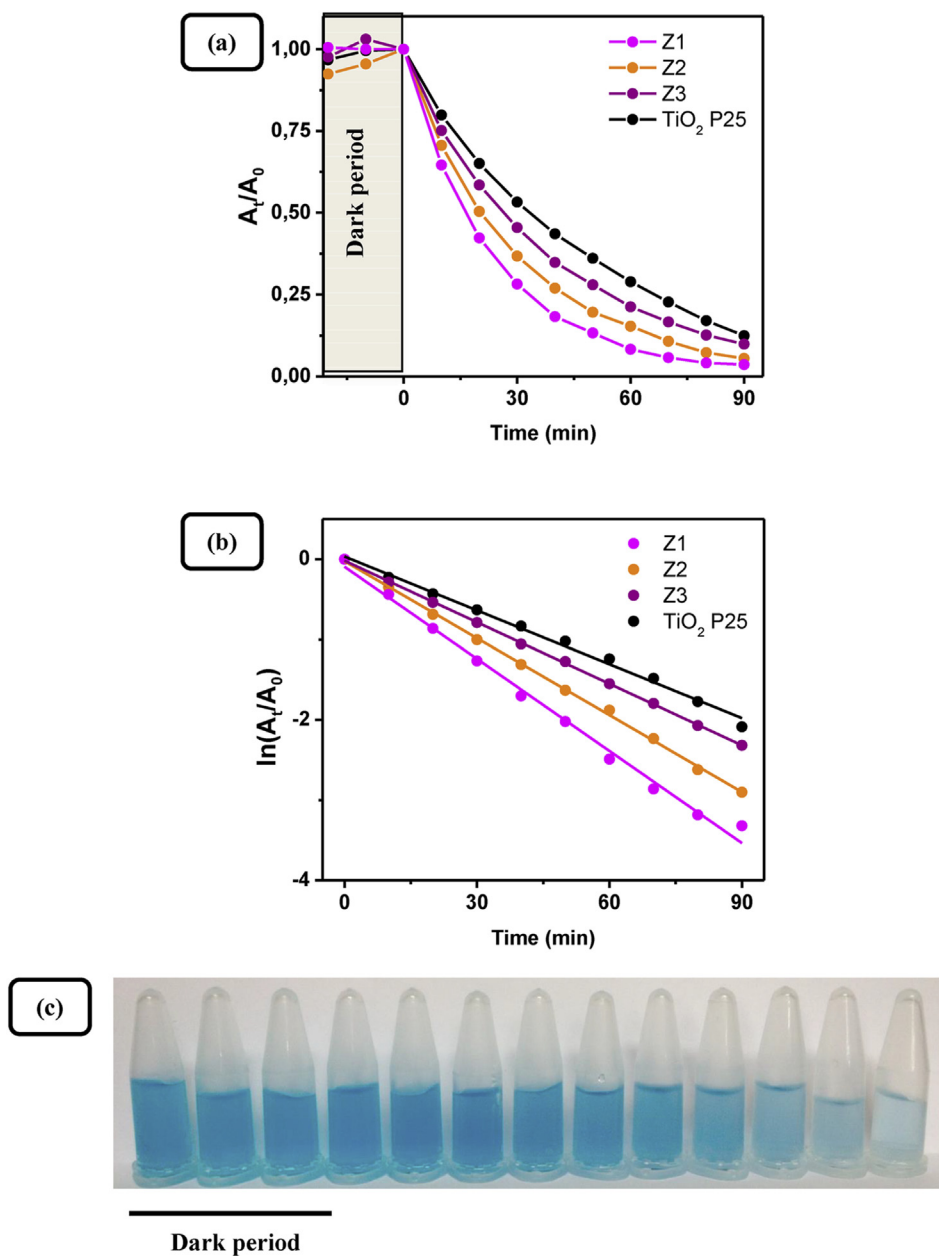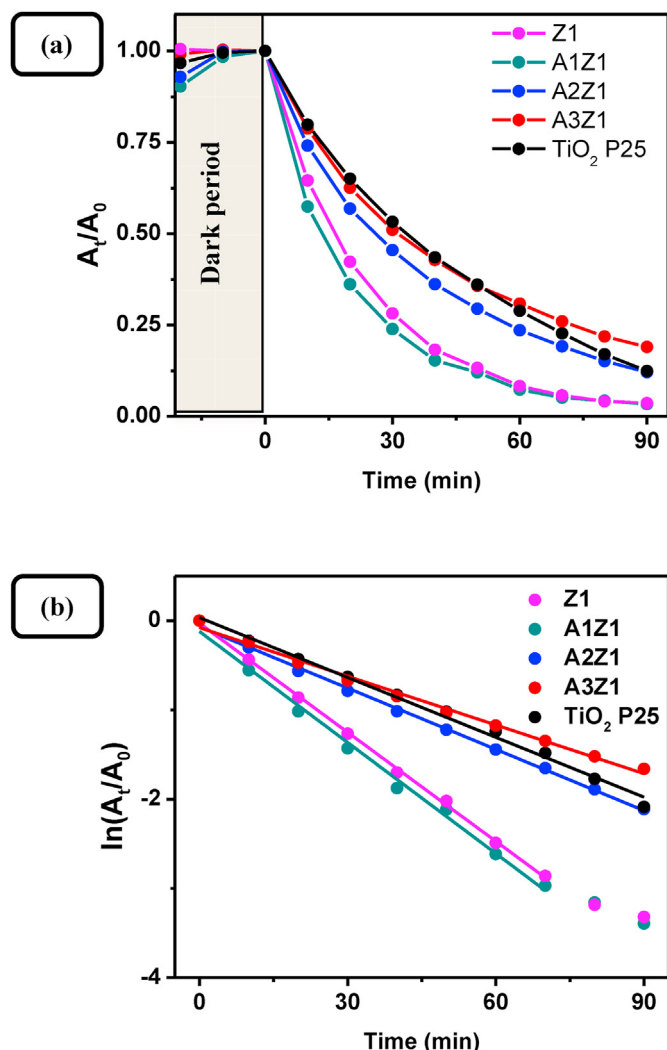
Figure 15. (a) Photocatalytic degradation of methylene blue dye (0.1 g, 2×10^{-5} M, pH ~7) from pure ZnO samples Z1, Z2, Z3 and TiO$_2$ P25 as a function of the time of irradiation; (b) Linearization in logarithmic scale showing a pseudo first order kinetics of degradation; (c) Digital photos of MB aliquotes taken at different times during photocatalysis by nanosized ZnO sample Z1.

Table 3. BET surface area values and kinetics characteristics of different ZnO and Au/ZnO photocatalysts (apparent reaction rate constants, k_{app}, and intrinsic activity, a_s) for photocatalytic degradation of MB under UV irradiation (R^2 represents the square of linear correlation coefficients).

Sample	S_{BET}, m^2 g^{-1}	k_{app}, min^{-1}	SD, min^{-1}	R^2	$a_s \times 10^3$, g m^{-2} min^{-1}
Z1	33	0.04071	0.0005	0.999	1.234
Z2	31	0.03194	0.0004	0.999	1.030
Z3	37	0.02554	0.0002	1.000	0.690
A1Z1	26	0.04146	0.0013	0.993	1.595
A2Z1	23	0.02288	0.0004	0.998	0.995
A3Z1	12	0.01818	0.0005	0.993	1.515
TiO$_2$ P25	-	0.02236	0.0006	0.993	-

Figure 16. (a) Photocatalytic degradation of methylene blue dye (0.1 g, 2 × 10^{-5} M, pH ~7) from pure ZnO sample Z1, Au-doped ZnO samples A1Z1, A2Z1, A3Z1, and TiO₂ P25 as a function of the time of irradiation; (b) Linearization in logarithmic scale showing a pseudo first order kinetics of degradation.

decreases gradually with increasing reaction time as a result of MB degradation. Moreover, no new peaks for organic intermediates appear during the photocatalytic process, thus suggesting that the photocatalysis of dye degradation, not only causes decoloration, but also complete oxidative decomposition occurs and no stable organic intermediates exist.
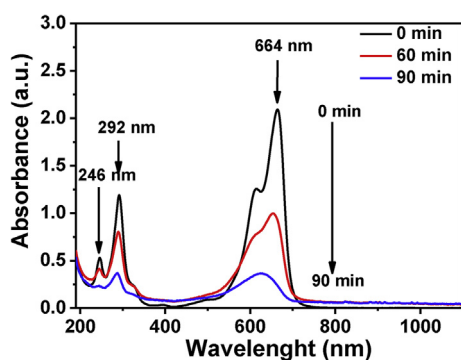
Figure 17. Variation of the absorption spectrum of MB solution during photocatalysis by nanosized ZnO sample Z1.

4. Conclusions

A new effective solution–solid synthesis method for preparation of nanocrystalline ZnO and Au-doped ZnO composite nanocrystals in starch matrix, characterized by simplicity, environmental compatibility and good performance, has been developed and optimized. Pure ZnO samples and Au/ZnO samples have been studied in detail in terms of crystal structure, size and shape, surface properties and morphology, optical properties. Spherical, polycrystalline nanoparticles of both zinc oxide and gold nanophases with a similar average diameter of 18–19 nm have been synthesized. The crystal lattice parameters of the semiconductor nanoparticles are not affected by the presence of gold, indicating that the metal does not enter it and no solid solutions are formed. Homogeneous distribution of the gold nanophase in the nanocomposite samples is observed. Highly porous morphology was found with comparable amounts of micro- and mesopores in all synthesized samples. The modification of nanocrystalline ZnO with gold nanocrystals strongly influences the porosity of nanocomposites - less micro- and mesopores are formed, which results in a reduced specific surface area.

The nanocrystalline ZnO synthesized show excellent photocatalytic activity demonstrated by the UV assisted photooxidative degradation of the model pollutant dye methylene blue (MB). The activity is higher than that of the commercial photocatalyst TiO₂ P25. The photocatalytic activity decreases with the increase in the gold content of nanocomposite nanocatalysts obviously due to the less developed surface of gold-doped ZnO nanocrystals providing less active sites for the photocatalytic degradation. The nanocomposite with lowest gold content 0.05 at.% demonstrates maximum specific (intrinsic) photocatalytic activity probably due to the achieved synergy in the electronic properties of both phases Au and ZnO. Complete oxidative degradation of the MB dye during the photocatalyzed process has been established, without obtaining stable organic intermediates.

Declarations

Author contribution statement

Boyan Peychev: Performed the experiments; Analyzed and interpreted the data; Wrote the paper.

Penka Vasileva: Conceived and designed the experiments; Analyzed and interpreted the data; Contributed reagents, materials, analysis tools or data; Wrote the paper.

Funding statement

Data availability statement

Data included in article/supp. material/referenced in article.

Declaration of interests statement

The authors declare no conflict of interest.

Additional information

No additional information is available for this paper.

References

[1] C. Burda, X. Chen, R. Narayanan, M.A. El-Sayed, Chemistry and properties of nanocrystals of different shapes, Chem. Rev. 105 (2005) 1025–1102.
[2] X. Chen, S.S. Mao, Titanium dioxide nanomaterials: synthesis, properties, modifications, and applications, Chem. Rev. 107 (2007) 2891–2959.

[3] T.H. Han, M.M. Khan, S. Kalathil, J. Lee, M.H. Cho, Simultaneous enhancement of methylene blue degradation and power generation in a microbial fuel cell by gold nanoparticles, Ind. Eng. Chem. Res. 52 (2013) 8174–8181.

[4] B. Nowack, Pollution prevention and treatment using nanotechnology, in: H. (Ed.), Nanotechnology. Volume 2: Environmental Aspects, WILEY-VCH Verlag GmbH & Co. KGaA, Weinheim, 2008, pp. 1–15.

[5] A. Sharma, P. Rao, R.P. Mathur, S.C. Ameta, Photocatalytic reactions of xylidine ponceau on semiconducting zinc oxide powder, J. Photochem. Photobiol. A: Chem. 86 (1995) 197–200.

[6] C.A. Gouvêa, F. Wypych, S.G. Moraes, N. Durán, P. Peralta-Zamora, Semiconductor-assisted photodegradation of lignin, dye, and kraft effluent by Ag-doped ZnO, Chemosphere 40 (2000) 427–432.

[7] S. Sakthivel, B. Neppolian, M.V. Shankar, B. Arabindoo, M. Palanichamy, V. Murugesan, Solar photocatalytic degradation of azo dye: comparison of photocatalytic efficiency of ZnO and TiO₂, Sol. Energy Mater. Sol. Cells 77 (2003) 65–82.

[8] S. Ahmed, M.G. Rasul, W.N. Martens, R. Brown, M.A. Hashib, Advances in heterogeneous photocatalytic degradation of phenols and dyes in wastewater: a review, Water Air Soil Pollut. 215 (2011) 3–29.

[9] M. Sleiman, D. Vildozo, C. Ferronato, J.M. Chovelon, Photocatalytic degradation of azo dye Metanil Yellow: optimization and kinetic modeling using a chemometric approach, Appl. Catal. B Environ. 77 (2007) 1–11.

[10] S. Chakrabarti, B.K. Dutta, Photocatalytic degradation of model textile dyes in wastewater using ZnO as semiconductor catalyst, J. Hazard Mater. 112 (2004) 269–278.

[11] M. Saquib, M.A. Tariq, M. Faisal, M. Muneer, Photocatalytic degradation of two selected dye derivatives in aqueous suspensions of titanium dioxide, Desalination 219 (2007) 301–311.

[12] C.G. Silva, W. Wang, J.L. Faria, Photocatalytic and photochemical degradation of mono-, di-and tri-azo dyes in aqueous solution under UV irradiation, J. Photochem. Photobiol. A: Chem. 181 (2006) 314–324.

[13] M. Stylidi, D.I. Kondarides, X.E. Verykios, Visible light-induced photocatalytic degradation of Acid Orange 7 in aqueous TiO₂ suspensions, Appl. Catal. B Environ. 47 (2004) 189–201.

[14] C. Su, B.Y. Hong, C.M. Tseng, Sol–gel preparation and photocatalysis of titanium dioxide, Catal. Today 96 (2004) 119–126.

[15] J. Sun, X. Wang, J. Sun, R. Sun, S. Sun, L. Qiao, Photocatalytic degradation and kinetics of Orange G using nano-sized Sn (IV)/TiO₂/AC photocatalyst, J. Mol. Catal. A: Chem. 260 (2006) 241–246.

[16] C. Hariharan, Photocatalytic degradation of organic contaminants in water by ZnO nanoparticles: Revisited, Appl. Catal. Gen. 304 (2006) 55–61.

[17] A.J. Walle, C.G. Van de Walle, Fundamentals of zinc oxide as a semiconductor, Rep. Prog. Phys. 72 (2009) 126501.

[18] O. Mekasuwandumrong, P. Pawinrat, P. Praserthdam, J. Panpranot, Effects of synthesis conditions and annealing post-treatment on the photocatalytic activities of ZnO nanoparticles in the degradation of methylene blue dye, Chem. Eng. J. 164 (2010) 77–84.

[19] A.B. Moghaddam, T. Nazari, J. Badraghi, M. Kazemzad, Synthesis of ZnO nanoparticles and electrodeposition of polypyrrole/ZnO nanocomposite film, Int. J. Electrochem. Sci. 4 (2009) 247–257.

[20] T. Shokuhfar, M.R. Vaezi, S.K. Sadrnezhad, A. Shokuhfar, Synthesis of zinc oxide nanopowder and nanolayer via chemical processing, Int. J. Nanomanuf. 2 (2008) 149–162.

[21] S.-J. Kim, D.-W. Park, Synthesis of ZnO nanopowder by thermal plasma and characterization of photocatalytic property, Appl. Chem. 11 (2007) 377–380.

[22] M.Y. Ge, H.P. Wu, L. Niu, J.F. Liu, S.Y. Chen, P.Y. Shen, Y.W. Zeng, Y.W. Wang, G.Q. Zhang, J.Z. Jiang, Nanostructured ZnO: from monodisperse nanoparticles to nanorods, J. Cryst. Growth 305 (2007) 162–166.

[23] J. Hambrock, S. Rabe, K. Merz, A. Birkner, A. Wohlfart, R.A. Fischer, M. Driess, Low-temperature approach to high surface ZnO nanopowders and a non-aqueous synthesis of ZnO colloids using the single-source precursor [MeZnOSiMe 3] 4 and related zinc siloxides, J. Mater. Chem. 13 (2003) 1731–1736.

[24] Y.J. Kwon, K.H. Kim, C.S. Lim, K.B. Shim, Characterization of ZnO nanopowders synthesized by the polymerized complex method via an organochemical route, J. Ceram. Process. Res. 3 (2002) 146–149.

[25] M.A. Gondal, M.A. Dastageer, A. Khalil, K. Hayat, Z.H. Yamani, Nanostructured ZnO synthesis and its application for effective disinfection of Escherichia coli micro organism in water, J. Nanopart. Res. 13 (2011) 3423–3430.

[26] M. Jitianu, D.V. Goia, Zinc oxide colloids with controlled size, shape, and structure, J. Colloid Interface Sci. 309 (2007) 78–85.

[27] R.S. Aga, R. Mu, Doping of polymers with ZnO nanostructures for optoelectronic and sensor applications, in: N. Lupu (Ed.), Nanowires: Science and Technology, Publisher BoD – Books on Demand, 2010, pp. 205–222.

[28] D. Visinescu, G. Patrinoiu, A. Tirsoaga, O. Carp, Polysaccharides route: a new green strategy for metal oxides synthesis, in: E. Lichtfouse, J. Schwarbauer, D. Robert (Eds.), Environmental Chemistry for a Sustainable World, Volume 1, Springer, Netherlands, 2012, pp. 119–169.

[29] O. Carp, D. Visinescu, G. Patrinoiu, A. Tirsoaga, C. Paraschiv, M. Tudose, Green synthetic strategies of oxide materials: polysaccharides-assisted synthesis. I. Polysaccharides roles in metal oxides synthesis, Rev. Roum. Chim. 55 (2010) 705–709.

[30] Y.J. Jang, C. Simer, T. Ohm, Comparison of zinc oxide nanoparticles and its nano-crystalline particles on the photocatalytic degradation of methylene blue, Mater. Res. Bull. 41 (2006) 67–77.

[31] N.S. Allen, M. Edge, J. Verran, J. Stratton, J. Maltby, C. Bygott, Photocatalytic surfaces: antipollution and antimicrobial effects, in: Nanotechnology, second ed., American Cancer Society, 2010, pp. 17–50.

[32] K.M. Parida, S.S. Dash, D.P. Das, Physico-chemical characterization and photocatalytic activity of zinc oxide prepared by various methods, J. Colloid Interface Sci. 298 (2006) 787–793.

[33] R. Kumar, D. Rana, A. Umar, P. Sharma, S. Chauhan, M.S. Chauhan, Ag-doped ZnO nanoellipsoids: potential scaffold for photocatalytic and sensing applications, Talanta 137 (2015) 204–213.

[34] C. Karunakaran, V. Rajeswari, P. Gomathisankar, Optical, electrical, photocatalytic, and bactericidal properties of microwave synthesized nanocrystalline Ag–ZnO and ZnO, Solid State Sci. 13 (2011) 923–928.

[35] F. Jamali-Sheini, R. Yousefi, D.S. Joag, M.A. More, Influence of chemical routes on optical and field emission properties of Au–ZnO nanowire films, Vacuum 101 (2014) 233–237.

[36] H. Chen, Y.M. Yeh, J.Z. Chen, S.M. Liu, B.Y. Huang, Z.H. Wu, S.L. Tsai, H.W. Chang, Y.C. Chu, C.H. Liao, Fabrication and characterizations of ZnO nanorods/Au nanoparticle composites on the electropolished Ti substrate, Thin Solid Films 549 (2013) 74–78.

[37] C. Tian, Q. Zhang, B. Jiang, G. Tian, H. Fu, Glucose-mediated solution–solid route for easy synthesis of Ag/ZnO particles with superior photocatalytic activity and photostability, J. Alloys Compd. 509 (2011) 6935–6941.

[38] Y. Xu, B. Yao, Y.F. Li, Z.H. Ding, J.C. Li, H.Z. Wang, Z.Z. Zhang, L.G. Zhang, H.F. Zhao, D.Z. Shen, Chemical states of gold doped in ZnO films and its effect on electrical and optical properties, J. Alloys Compd. 585 (2014) 479–484.

[39] P. Bažant, Z. Kožáková, O. Hudeček, M. Machovský, M. Pastorek, I. Kuřitka, Composite material based on hybrid micro-sized Ag-ZnO filler for antibacterial applications, Nanocon (2011) 459–465.

[40] R. Kavitha, S.G. Kumar, A review on plasmonic Au-ZnO heterojunction photocatalysts: preparation, modifications and related charge carrier dynamics, Mater. Sci. Semicond. Process. 93 (2019) 59–91.

[41] P. Vasileva, Synthesis and characterization of ZnO nanocrystals in starch matrix, Mater. Sci., Nonequilib. Phase Transform. 2 (2016) 26–29.

[42] Z. Xingfu, H. Zhaolin, F. Yiqun, C. Su, D. Weiping, X. Nanping, Microspheric organization of multilayered ZnO nanosheets with hierarchically porous structures, J. Phys. Chem. C 112 (2008) 11722–11728.

[43] W.L. Ong, S. Natarajan, B. Kloostra, G.W. Ho, Metal nanoparticle-loaded hierarchically assembled ZnO nanoflakes for enhanced photocatalytic performance, Nanoscale 5 (2013) 5568–5575.

[44] G. Zhang, X. Shen, Y. Yang, Facile synthesis of monodisperse porous ZnO spheres by a soluble starch-assisted method and their photocatalytic activity, J. Phys. Chem. C 115 (2011) 7145–7152.

[45] J. Tang, Z. Zou, J. Ye, Photocatalytic decomposition of organic contaminants by Bi₂WO₆ under visible light irradiation, Catal. Lett. 92 (2004) 53–56.

[46] L. Zhang, W. Wang, L. Zhou, H. Xu, Bi₂WO₆ nano-and microstructures: shape control and associated visible-light-driven photocatalytic activities, Small 3 (2007) 1618–1625.

[47] S. Monticone, R. Tufeu, A.V. Kanaev, Complex nature of the UV and visible fluorescence of colloidal ZnO nanoparticles, J. Phys. Chem. B 102 (1998) 2854–2862.

[48] Y.L. Wu, A.I.Y. Tok, F.Y.C. Boey, X.T. Zeng, X.H. Zhang, Surface modification of ZnO nanocrystals, Appl. Surf. Sci. 253 (2007) 5473–5479.

[49] L.L. Wu, Y.S. Wu, X.R. Pan, F.Y. Kong, Synthesis of ZnO nanorod and the annealing effect on its photoluminescence property, Opt. Mater. 28 (2006) 418–422.

[50] M.J. Height, S.E. Pratsinis, O. Mekasuwandumrong, P. Praserthdam, Ag–ZnO catalysts for UV-photodegradation of methylene blue, Appl. Catal. B Environ. 63 (2006) 305–312.

[51] Y. Cheng, W. Wang, L. Yao, J. Wang, Y. Liang, J. Fu, Insights into charge transfer and solar light photocatalytic activity induced by the synergistic effect of defect state and plasmon in Au nanoparticle decorated hierarchical 3D porous ZnO microspheres, Appl. Surf. Sci. 494 (2019) 959–968.

[52] A.K. Zak, W.A. Majid, M. Darroudi, R. Yousefi, Synthesis and characterization of ZnO nanoparticles prepared in gelatin media, Mater. Lett. 65 (2011) 70–73.

[53] B. Jurca, A. Tirsoaga, A. Ianculescu, O. Carp, Influence of the synthesis parameters on the thermal behavior of some ZnO–starch composites, J. Therm. Anal. Calorim. 115 (2014) 495–501.

[54] P. Arsana, C. Bubpa, W. Sang-Aroon, Photocatalytic activity under solar irradiation of silver and copper doped zincoxide: photodeposition versus liquid impregnation methods, J. Appl. Sci. (Faisalabad) 12 (2012) 1809–1816.

[55] M.A. Behnajady, N. Modirshahla, R. Hamzavi, Kinetic study on photocatalytic degradation of CI Acid Yellow 23 by ZnO photocatalyst, J. Hazard Mater. B133 (2006) 226–232.

[56] N. Daneshvar, D. Salari, A.R. Khataee, Photocatalytic degradation of azo dye acid red 14 in water on ZnO as an alternative catalyst to TiO₂, J. Photochem. Photobiol. A 162 (2004) 317–322.

[57] J.J. Wu, C.H. Tseng, Photocatalytic properties of nc-Au/ZnO nanorod composites, Appl. Catal. B Environ. 66 (2006) 51–57.

[58] A. Senthilraja, B. Subash, B. Krishnakumar, D. Rajamanickam, M. Swaminathan, M. Shanthi, Synthesis, characterization and catalytic activity of co-doped Ag–Au–ZnO for MB dye degradation under UV-A light, Mater. Sci. Semicond. Process. 22 (2014) 83–91.